Journal of Electroanalytical Chemistry 996 (2025) 119372

Contents lists available at ScienceDirect

Journal of Electroanalytical Chemistry

journal homepage: www.elsevier.com/locate/jelechem

On the implications of silver addition for the structure and anodic performance of polyaniline/$(FeCoNiCrMn)_3O_4$ high-entropy oxide composite used in lithium-ion batteries

Arezoo Jari [a], Abbas Bahrami [a,*], Masoud Panjepour [a], Maryam Yazdan Mehr [b]

[a] Department of Materials Engineering, Isfahan University of Technology, Isfahan 84156-83111, Iran
[b] Faculty EEMCS, Delft University of Technology, Mekelweg 4, 2628 CD Delft, the Netherlands

ARTICLE INFO

Keywords:
High-entropy oxide
Silver
Spinel-structured
Polyaniline coating
Lithium-ion battery anodes

ABSTRACT

This study focuses on enhancing the performance of $(FeCoNiCrMn)_3O_4$ high-entropy oxide (HEO) anodes for lithium-ion batteries (LIBs) by adding polyaniline (PANI) and silver (Ag). The HEO was synthesized using a solid-state method, involving ball milling and high-temperature heat treatment, which resulted in a stable spinel structure. To further improve its properties, the HEO powder was coated with a PANI-Ag layer via oxidative polymerization and the addition of silver nanoparticles, enhancing conductivity and mitigating lithium dendrite formation. The HEO-P-Ag composite demonstrated significant improvements compared to the unmodified HEO. The initial discharge capacity of HEO-P-Ag was 1050.8 mA hg^{-1}, while its charge capacity was 711 mA h g^{-1}, both of which exceeded the corresponding values of the bare HEO (827 mA h g^{-1} for discharge and 445 mA h g^{-1} for charge). Additionally, the composite also exhibited good rate capability, achieving a reversible capacity of 265 mA h g^{-1} at a rate of 1C. Electrochemical impedance spectroscopy (EIS) confirmed that the PANI-Ag coating effectively reduced charge transfer resistance and enhanced lithium ion diffusion. Accordingly, these findings indicate that HEO-P-Ag could serve as a promising anode material for high-performance LIBs, delivering high capacity, improved rate capability, and stable cycling performance.

1. Introduction

To address the challenges imposed by global warming and keep up with societal developments, there is increasing attention on portable electric devices, electric vehicles, and hybrid electric vehicles that utilize batteries for energy storage [1–3]. Consequently, effort are being made to develop battery technologies that provide both high capacity and high power to meet the growing demands for energy storage [4]. Among the various energy storage methods available, lithium-ion batteries (LIBs) stand out as a leading technology for rechargeable energy storage and conversion [5,6]. Their high energy density, high power density, high output voltage, cost-effectiveness, and long cycle life all contribute to their valued performance in the field [7–9]. In fact, among the different components of a battery system, anode materials play an essential role. The currently available commercial graphite anodes are insufficient to fully meet the demands for high-energy LIBs due to their relatively low theoretical capacity (372 mA h g^{-1}) and associated safety risks, particularly those related to lithium dendrite formation [10]. Consequently, it is essential to focus on the development of novel and innovative electrode materials and structures that enhance both theoretical capacities and charging/discharging rates as alternatives to graphite-based materials. Several active materials with higher theoretical capacities have been identified as potential replacements for graphite. In particular, the design of high-entropy oxides (HEOs) as anode materials represents a promising recent development that is gaining attention in the field of LIBs [11–15]. Recent investigations have demonstrated that elemental synergy within HEOs plays a critical role in forming stable, self-assembled metal-oxide nanostructures that facilitate both electron transport and Li^+ storage. Wang et al. [16] reported a (MgCoNiCuZn)O system where the coexistence of a 3D metallic network and semi-coherent oxide nanophases enabled high capacity and structural stability. According to Boltzmann Eq. [17] as shown in Eq. (1), materials with a $\Delta S_{mix} \geq 1.5R$ are classified as high-entropy [18–20].

$$\Delta S_{config} = -R\left(\sum_{i=1}^{N} x_i \ln x_i\right) \quad (1)$$

* Corresponding author.
E-mail address: a.n.bahrami@iut.ac.ir (A. Bahrami).

https://doi.org/10.1016/j.jelechem.2025.119372
Received 22 April 2025; Received in revised form 18 July 2025; Accepted 30 July 2025
Available online 5 August 2025

where R represents the gas content, xi represents the mole fractions of the metal cations, and N is the number of cation species present in the composition. The high configurational entropy of HEOs contributes to the microstructural stability, allowing the lattice structure to remain stable during extended cycling. This is a major upside, as it results in minimal volume changes during operation.

Incorporating conductive polymers, such as polypyrrole (PPy) and polyaniline (PANI), with electrode materials has led to significant improvements in electrochemical performance of anode materials. These polymers are gaining attention in the field of rechargeable batteries due to their superior electrical conductivity, structural stability, and ease of synthesis [21–23]. A noteworthy example is the development of Sb_2MoO_6@PANI nanorods by Yang et al.'s [24] for use as sodium-ion battery anodes. This innovation demonstrates improved cycling stability and rate capability compared to bare Sb_2MoO_6, attributable to the conductive and stable PANI coating. Further, Jeong et al. [25] and Gao et al. [26] have incorporated silver (Ag) as a significant additive in the structure of anode materials, resulting in enhanced electrochemical performance. The incorporation of Ag particles yielded several advantages, including ultrafast electron transport, decreased charge and capacitance resistance, and effective suppression of Li dendrite formation. Previous research has demonstrated HEO's potential as an exceptional anode material for batteries, given its promising characteristics as a single-phase solid-solution oxide, although further investigation is certainly necessary [27–29].

Building on previous studies, this research focuses on the fabrication of a HEO/PANI/Ag composite electrode through a simple and scalable process. While high-entropy oxides (HEOs) have shown promising potential as anode materials for lithium-ion batteries (LIBs), existing studies do not systematically explore strategies to overcome their inherent limitations, such as poor conductivity and susceptibility to structural degradation during cycling. Integrating HEOs with conductive polymers like polyaniline (PANI) and metallic nanoparticles such as silver (Ag) presents an innovative approach to enhancing their electrochemical performance, addressing critical gaps in understanding their combined influence on electrochemical behavior. Resolving these challenges is essential for advancing high-capacity and durable anode materials for next-generation LIBs. Additionally, Liu et al. [30] developed a hollow multishelled HEO architecture exhibiting impressive capacity retention and mechanical integrity under cycling, further confirming the potential of structural engineering in HEO-based anodes.

By leveraging the unique properties of PANI and Ag, this study introduces a novel HEO-PANI-Ag composite structure aimed at enhancing lithium storage performance by improving conductivity, increasing rate capability, and stabilizing the electrode during cycling. To systematically optimize its characteristics, this research investigates the effects of Ag incorporation on key electrochemical parameters, including charge-transfer resistance, lithium-ion diffusion, and cycling stability, providing new insights into the design of high-performance anode materials for next-generation LIB applications.

2. Materials and experimental methods

2.1. Chemicals and synthesis process

Fe_2O_3, Cr_2O_3, NiO, Co_3O_4, and MnO_2 (all sourced from Merck, $\leq$ 99 %) were homogeneously mixed in equimolar ratios to synthesize $(FeCoNiCrMn)_3O_4$. The synthesis process was generally conducted in

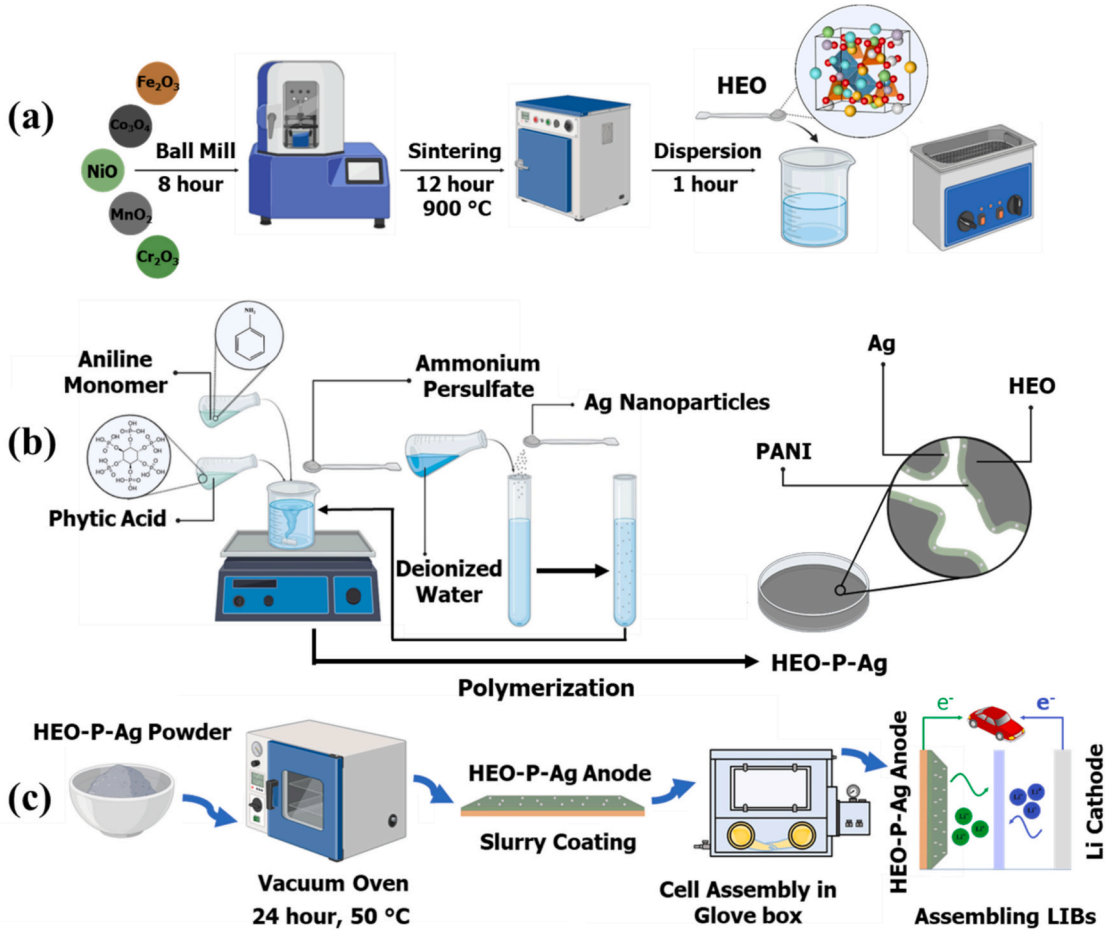

Fig. 1. Schematic illustration of the preparation of (a) HEO, (b) HEO-P-Ag, and (c) half-cell assembly.

three stages, as illustrated in the schematic shown in Fig. 1.

a) Initially, the mixture was then milled at 250 rpm for 8 h in a ball mill. Subsequently, the resulting oxide mixture was heat-treated at 900 °C for 12 h and allowed to cool naturally to room temperature. Before synthesis, configurational entropy values were determined using Eq. 1. The calculated S_{conf} value of 1.61R for the synthesized HEOs indicates the formation of a high-entropy oxide mixture. A total of 0.5 g of synthesized HEO powder was dispersed in 100 mL of deionized water using ultrasonic dispersion for 1 h.

b) Following this, the synthesized HEO powder was combined with 0.15 mL aniline monomer and 0.3 mL of a 50 % phytic acid solution The resulting mixture was stirred for approximately 12 h. At that point, 0.2 g ammonium persulfate (APS) was added into the mixture, initiating an oxidative polymerization reaction under continuous stirring. After 1 h, 0.095 g of Ag nanoparticles suspended in 10 mL of deionized water was incorporated into the mixture. Three hours later, the mixture was filtered and washed several times with deionized water and ethanol.

c) The final sample was then dried overnight in a vacuum oven at 50 °C and transferred to an argon-filled glove box for further use.

For the sake of comparison, pure PANI and HEO-PANI (HEO-P) were also synthesized following the same procedure.

2.2. Anode preparation and electrochemical measurements

The preparation of the anode involved creating a homogenous slurry consisting of 80 wt% active material, 10 wt% carbon black (Super P), and 10 wt% polyvinylidene fluoride (PVDF) binder dispersed in *N*-methyl-2-pyrrolidone. This slurry was then applied to copper foil using a doctor blade and subsequently dried at 50 °C for 24 h under vacuum. HEO and HEO-P-Ag served as the active materials, with a loading mass of approximately 1.5 mg cm^{-2}, in the half-cell setup. This configuration included a lithium metal foil as the counter/reference electrode and a Celgard 2325 membrane (comprising three layers of PP/PE/PP) as the separator. The electrochemical properties were examined using CR2032 coin cells, which were assembled in an argon-filled glove box (SMART LINE) that maintained humidity and oxygen levels below 0.1 ppm.

The electrolyte consisted 1 M lithium hexafluorophosphate ($LiPF_6$) dissolved in a volumetric ratio mixture of ethylene carbonate (EC), ethyl methyl carbonate (EMC), and dimethyl carbonate (DEC) at a ratio of 1:1:1. Electrochemical impedance spectroscopy (EIS) was carried out using an SP50e Bio Logic electrochemical workstation, operating over a frequency range of 0.01 Hz to 100 kHz. Galvanostatic tests were conducted at ambient temperature within a voltage range of 0.01–3 *V* versus Li/Li^+, utilizing a NEWARE battery testing system at various current densities. Cyclic voltammetry (CV) was carried out using a PARSTAT 3000 A potentiostat over a potential window of 0.01–3.0 V at a sweep rate of 0.1 mV s^{-1}.

2.3. Structural characterization

To investigate the phase and crystalline structure of samples, X-ray diffraction (XRD) analysis was performed using a Philips diffractometer operating at 40 kV. The experiments employed Cu Kα radiation (λ = 1.5406 Å) to scan the samples at a rate of 0.05°/s over the 2θ range of 20–80°. Further, Fourier-transform infrared (FT-IR) spectra were acquired using a Bruker Tensor 27 spectrometer, spanning a wavenumber range from 300 to 6000 cm^{-1}.

Morphological and chemical analyses were performed using scanning electron microscopy (SEM, Philips XI30) equipped with an energy-dispersive X-ray spectroscopy (EDS, Seron AIS 2300) detector. Additionally, further structural characterization, including morphology, high-resolution transmission electron microscopy (HRTEM), EDS, and selected area electron diffraction (SAED), was carried out through transmission electron microscopy (TEM, JEOL JSM-6710F) at an accelerating voltage of 300 kV. The morphology and microstructure of the HEO and HEO-P-Ag anodes were characterized before and after the lithiation/delithiation process using a field-emission scanning electron microscope (FESEM, FEI QUANTA FEG-450).

3. Results and discussion

To determine the phase and crystal structure of the raw powder mixtures, HEO and HEO-P-Ag, X-ray diffraction (XRD) analysis was conducted, as demonstrated in Fig. 2. Upon heat treatment at 900 °C, the resulting HEO (Fig. 2(b)) was found to exhibit a cubic spinel structure corresponding to the $Fd\bar{3}m$ space group (COD No. 9005841), which corroborates its high degree of crystallinity and purity. Moreover, the XRD pattern of HEO revealed no additional diffraction peaks attributable to other transition metal oxide, indicating a high level of phase purity. Fig. 2(c) shows that the XRD pattern of HEO-P-Ag closely resembles that of the spinel structure. This similarity indicates that the crystalline structure remains unchanged after modification with PANI and Ag, thereby confirming the stability of HEO-P-Ag powder. Both samples displayed similar phase structures characterized by low and flat backgrounds, with diffraction peaks at 18.40°, 30.27°, 35.65°, 37.30°, 43.34°, 53.77°, 57.33°, 63°, 71.44°, 74.51°, and 75.52°. These peaks correspond to the (111), (220), (311), (222), (4 0 0), (4 2 2), (5 1 1), (4 4 0), (6 2 0), (5 3 3), and (6 2 2) planes of the spinel structure. Recent studies [31], indicate that the spinel structure facilitates effective transport of Li^+. Additionally, the presence of oxygen vacancies, resulting from various cation valence states within the spinel HEO, enhances Li^+ conduction.

Although lower calcination temperatures can induce spinel phase formation in HEOs, a temperature of 900 °C was selected to ensure complete crystallization, high phase purity, and robust structural integrity required for high-performance electrochemical applications. This elevated temperature also enhances cationic diffusion and homogeneity, which are essential for achieving stable entropy-stabilized oxide phases [32].

Fourier-transform infrared (FT-IR) spectroscopy is a highly valuable analytical tool used to evaluate the structure of newly synthesized materials. To confirm the presence of Ag and PANI within the composite structure, FT-IR analysis was performed, with the resulting spectra displayed in Fig. 3. A notable absorption peak observed near 3440 cm^{-1} for Ag, PANI, and HEO-P-Ag can be attributed to hydroxyl (-OH) groups. Particularly, the spectrum profile of HEO-P-Ag differs markedly from that of pure HEO, indicating distinct chemical functionalities. The characteristic absorption bands of PANI are also observed in the

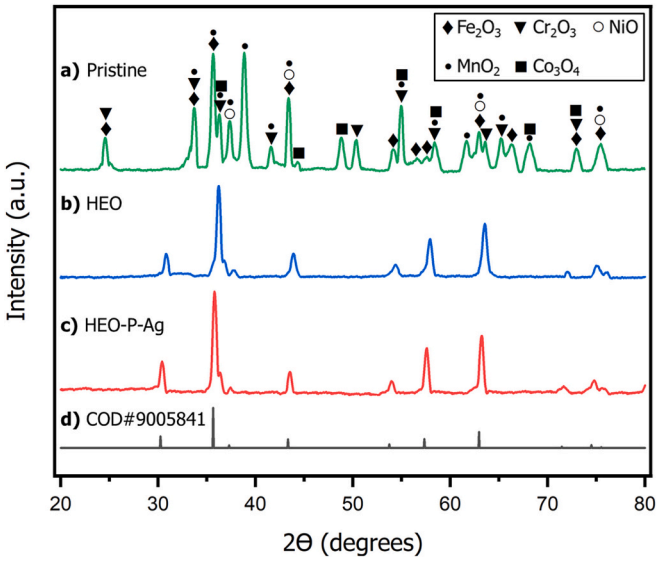

Fig. 2. XRD patterns of (a) raw powder mixtures, (b) HEO particles, (c) HEO modified by PANI and Ag, and (d) standard XRD pattern of HEO.

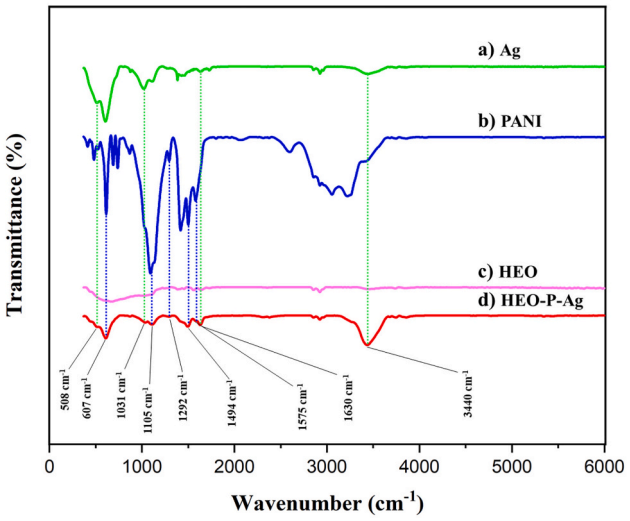

Fig. 3. FTIR spectra of (a) Ag, (b) PANI, (c) HEO, and (d) HEO-P-Ag.

spectrum of HEO-P-Ag, such as N = Q = N, C═C, and C═N stretching vibrations at 1575, 1494, and 1292 cm^{-1}, respectively. Additionally, peaks at 1105 and 607 cm^{-1} are associated with both in-plane and out-of-plane C—H bending vibrations of para-disubstituted benzene rings. This further supports the incorporation of conductive PANI into the composite. Furthermore, characteristic Ag bands are visible in the HEO-P-Ag spectrum, with a peak at 1630 cm^{-1} indicating the presence of an amide group and a band at 1031 cm^{-1} assigned to C—N bonds of aliphatic amines in the formed particles [33–35]. The porous structure of the PANI layer, combined with the presence of conductive Ag, is expected to significantly enhance the electrochemical performance of the anode material.

Figure 4(a) and (b) show the SEM and TEM micrographs of $(FeCoNiCrMn)_3O_4$ after heat treatment at 900 °C, revealing numerous particles with diameters ranging from 1 to 10 μm. This appears that particle size has increased as a result of the high-temperature thermal treatment. Recent research [36] posits that use of nanoparticles as electrodes in lithium-ion batteries could significantly enhance the number of active sites available for charge storage. This increased accessibility of charge storage sites may lead to enhanced capacity, improved high-rate performance, and better reversibility. To minimize aggregation effects, powders were milled briefly prior to the preparation of the electrodes. HRTEM and SAED techniques were employed for a more detailed microstructural assessments of HEO. The HRTEM images presented in Fig. 4(c-e) reveal lattice spacing measurements of 0.253, 0.201, and 0.48 nm, which correspond to the (3 1 1), (200), and (1 1 1) lattice planes of the spinel structure. The SAED pattern in Fig. 4(f) exhibits distinct circular diffraction rings, which indicate the polycrystalline nature of the synthesized sample. The diffraction rings corresponding to (1 1 1), (2 2 0), (2 2 2), and (0 4 4) planes of a face-centered cubic (FCC) structure can be identified from the center to the outer layer in this figure aligning with the XRD patterns. Furthermore, TEM-EDS elemental mapping was performed within a specific region (Fig. 4(g)), confirming a homogeneous distribution of elements, Fe, Co, Ni, Cr, Mn, and O, in the high entropy oxide, with no evident elemental segregation observed. This finding underscores the critical role of the high-entropy stabilization effect in establishing a uniform phase.

The elemental distribution was also examined using EDS analyses and elemental mappings of HEO and HEO-P-Ag compositions, as shown in Fig. 5. The results demonstrated a high degree of uniformity in the distribution of Fe, Co, Ni, Cr, Mn, and O elements. Furthermore, the presence of Ag, C, and N peaks in the HEO-P-Ag sample confirmed the successful and homogenous coverage of HEO particles with PANI and Ag in the modified sample.

It is important to note that while equimolar amounts of Fe_2O_3, Cr_2O_3, NiO, Co_3O_4, and MnO_2 were used in the synthesis process, this does not translate to equimolar cation concentrations in the final product due to the different stoichiometries of the precursor oxides. Furthermore, minor deviations in the measured atomic percentages from the ideal values are expected, given the semi-quantitative nature and surface sensitivity of EDS. Nonetheless, the TEM-EDS elemental mapping (Fig. 4(g)) confirms uniform elemental distribution, consistent with high-entropy solid solution behavior.

Galvanostatic cycling between 0.01 and 3.0 *V* vs. Li/Li^+ was conducted on coin cells at room temperature to evaluate the lithium storage performance of HEO-P-Ag, HEO—P, and HEO electrodes. The discharge/charge curves for the HEO-P-Ag, HEO-P and HEO samples at a C-rate of C/10 (where 1C = 2 A g^{-1}) can be observed in Fig. 6 (a-c). Each sample exhibits slopes rather than plateaus during the discharge process, which are related to the multiple-step reaction mechanisms characteristic of HEOs. HEO-P-Ag demonstrated an initial discharge capacity of 1050.8 mA h g^{-1} and a charge capacity of 711 mA h g^{-1}, both of which surpass those of HEO-P and HEO. For HEO—P, the discharge and charge capacities were 965 mA h g^{-1} and 612 mA h g^{-1}, respectively, while HEO showed 827 mA h g^{-1} for discharge and 445 mA h g^{-1} for charge.

The coulombic efficiency of HEO-P-Ag was 67.66 % during the first cycle, a result of electrolyte decomposition, irreversible solid-electrolyte interphase (SEI) film formation, and structural rearrangement. However, the coulombic efficiency increased to approximately 80 % from the second cycle onward, demonstrating excellent reversible lithium storage capabilities of HEO as an anode material for LIBs. The initial capacity loss during the first few cycles arises from irreversible processes, including SEI formation, structural changes in the HEO particles, and lithium trapping. These effects, common in conversion-type anodes, are amplified by early-cycle volume changes. The PANI-Ag coating plays a key role in mitigating this degradation, leading to greater structural stability and improved efficiency in subsequent cycles.

The rate properties of the electrodes were evaluated at C/10, C/5, C/3, C/2, and 1C as illustrated in Fig. 6(d-f). As expected, HEO-P-Ag exhibited better rate capability compared to HEO-P and HEO. Specifically, HEO-P-Ag achieved a reversible capacity of 529 mA h g^{-1} at C/5 and a specific capacity of 252 mA h g^{-1} at 1C. Upon resetting the C-rate from 1C to C/5, the capacity reverts to 328 mA h g^{-1}, indicating the structural stability of the HEO-P-Ag electrode and its ability to accommodate significant changes in current density. The discharge–charge curves of HEO-P showed a capacity of 459 mA h g^{-1} at C/5 and 181 mA h g^{-1} at 1C, while HEO showed 174 mA h g^{-1} at C/5 and 45 mA h g^{-1} at 1C. The improved rate performance can be attributed to the efficient charge transfer characteristics of the structurally stable HEO-P-Ag electrode. The rate performance of electrode materials is significantly influenced by their electronic conductivity and diffusion pathways. The impressive rate capability of HEO-P-Ag can be attributed to the enhanced electrical conductivity derived from the PANI layer, which improves the charge transfer and storage properties of HEO. The introduction of a small amount of atoms, such as Ag, into the electrode material increases the Li^+ ion diffusion coefficient (D_{Li^+}). Consequently, the design of HEO-P-Ag as a promising anode material leads to improved electronic conductivity and a greater number of electrochemically active components compared to HEO.

To evaluate the long-term cycling stability of the HEO-P-Ag electrode, additional galvanostatic cycling was conducted at a current density of 200 mA g^{-1} for 150 cycles (Fig. 6(g)). The electrode maintained a stable capacity of over 400 mA h g^{-1} throughout the test, indicating minimal capacity fading. This result confirms the excellent structural robustness and electrochemical durability of the Ag–PANI coating.

To further investigate the redox behavior and reaction kinetics of the HEO-P-Ag electrode, cyclic voltammetry (CV) measurements were conducted at a scan rate of 0.1 mV s^{-1} for the first three cycles, as shown in Fig. 6 (h). The CV curves display multiple anodic and cathodic peaks

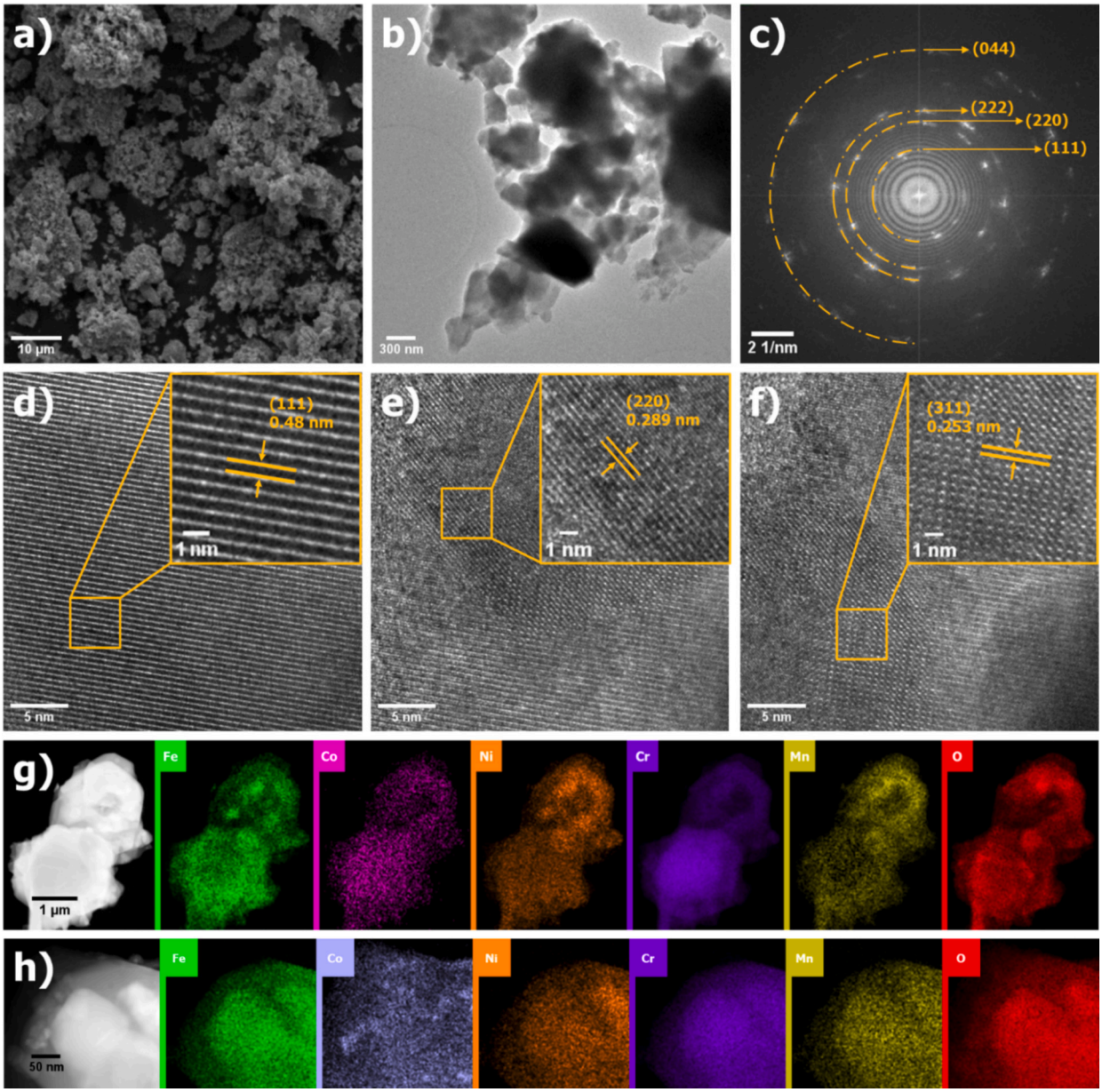

Fig. 4. (a) SEM image, (b) TEM image, (c) SAED pattern, (d-f) HRTEM images, and (g, h) elemental mapping images of the HEO particles.

associated with Li^+ insertion and extraction. During the first cathodic scan, a strong and well-defined peak appears at approximately 0.55 V, corresponding to the stepwise reduction of transition metal oxides, and SEI formation. In the anodic scan, the current rises steadily around 1.0–1.2 V, and broad overlapping oxidation peaks between 1.2 and 2.5 V can be ascribed to the reversible oxidation of Fe, Co, Ni, Cr, and Mn to their respective oxides. From the second cycle onward, the CV curves exhibit significant overlap, indicating excellent electrochemical reversibility and stable Li^+ insertion/extraction behavior.

Table 1 provides a comparative overview of HEO-P-Ag and other recently reported high-entropy oxide-based anode materials. While the others show competitive performance, HEO-P-Ag demonstrates superior capacity and rate capability. This enhanced performance stems from the synergistic contribution of the conductive polyaniline (PANI) coating and well-dispersed silver (Ag) nanoparticles. The PANI layer forms a flexible, conductive network that enhances electron transport and buffers mechanical stress from volume changes during cycling. Meanwhile, Ag nanoparticles significantly reduce charge-transfer resistance and accelerate lithium-ion diffusion across the electrode–electrolyte interface. Together, these effects lead to better electrochemical kinetics, more stable SEI formation, and suppressed electrode pulverization. This structural integrity and fast ion/electron transport enable the HEO-P-Ag composite to maintain high capacity and stability, making it a strong candidate for high-performance lithium-ion battery applications.

Electrochemical impedance spectroscopy was employed to further evaluate the improved electrochemical performance of HEO-P-Ag in comparison to HEO, with a focus on electrical conductivity and Li^+ transfer behavior. Fig. 7(a) illustrates the Nyquist plots for the HEO-P-Ag, HEO—P, and HEO electrodes prior to cycling, with frequencies measurements spanning from 0.01 Hz to 100 kHz. Each Nyquist plot exhibits a semicircle in the medium-high frequency region and a straight line in the low-frequency region. The semicircle represents the impedance of the SEI film (R_{SEI}) and the charge transfer resistance (R_{ct}), while the straight line corresponds to the Warburg impedance (Z_w), which is associated with Li^+ diffusion in the electrode. An equivalent circuit was used to simulate the Nyquist plots. As shown in this figure, the semicircle diameter of HEO-P-Ag is significantly smaller than that of HEO-P and HEO, indicating a reduced charge-transfer resistance in HEO-P-Ag. The

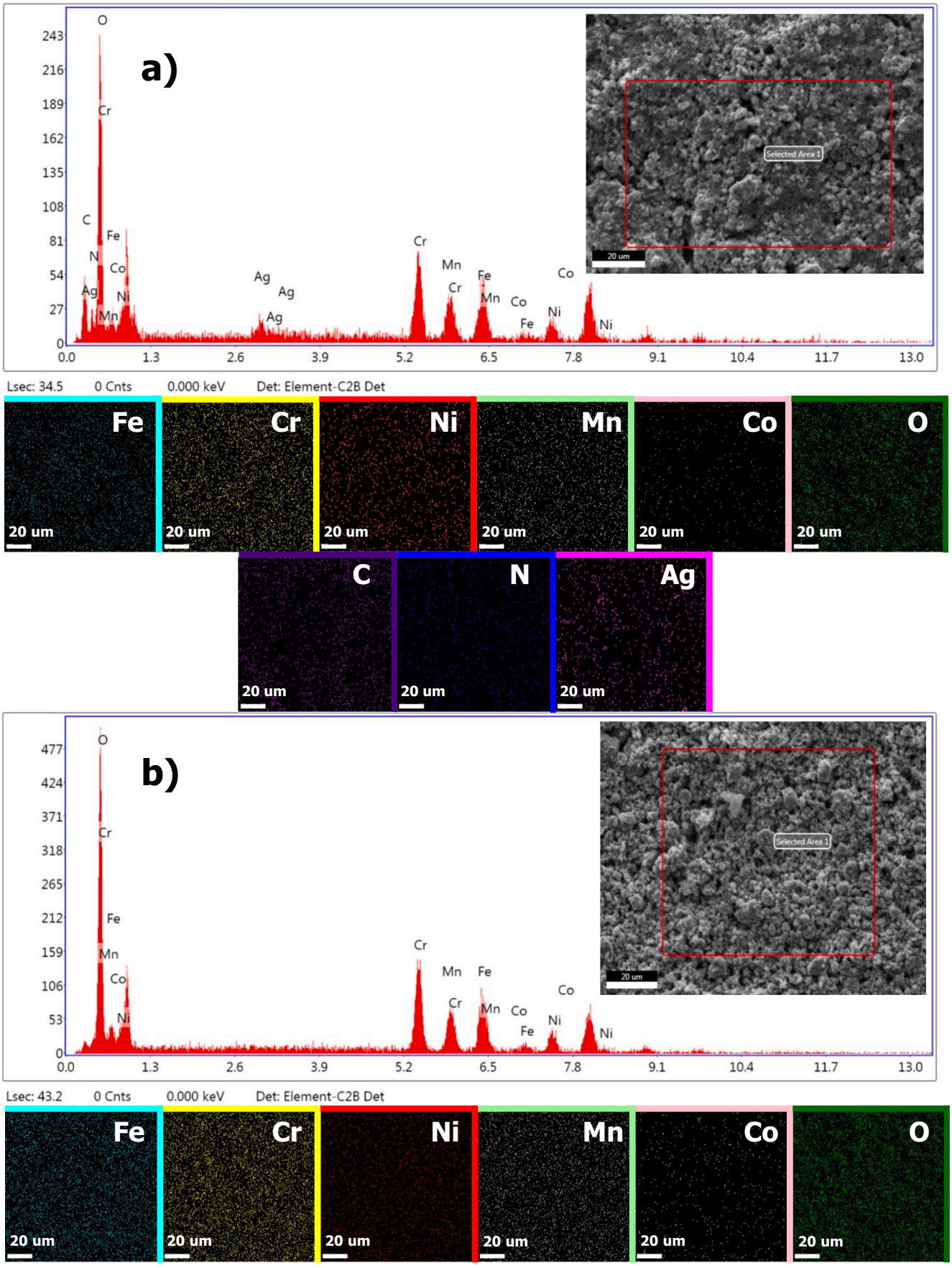

Fig. 5. EDS analysis and elemental mapping of (a) HEO-P-Ag and (b) HEO particles.

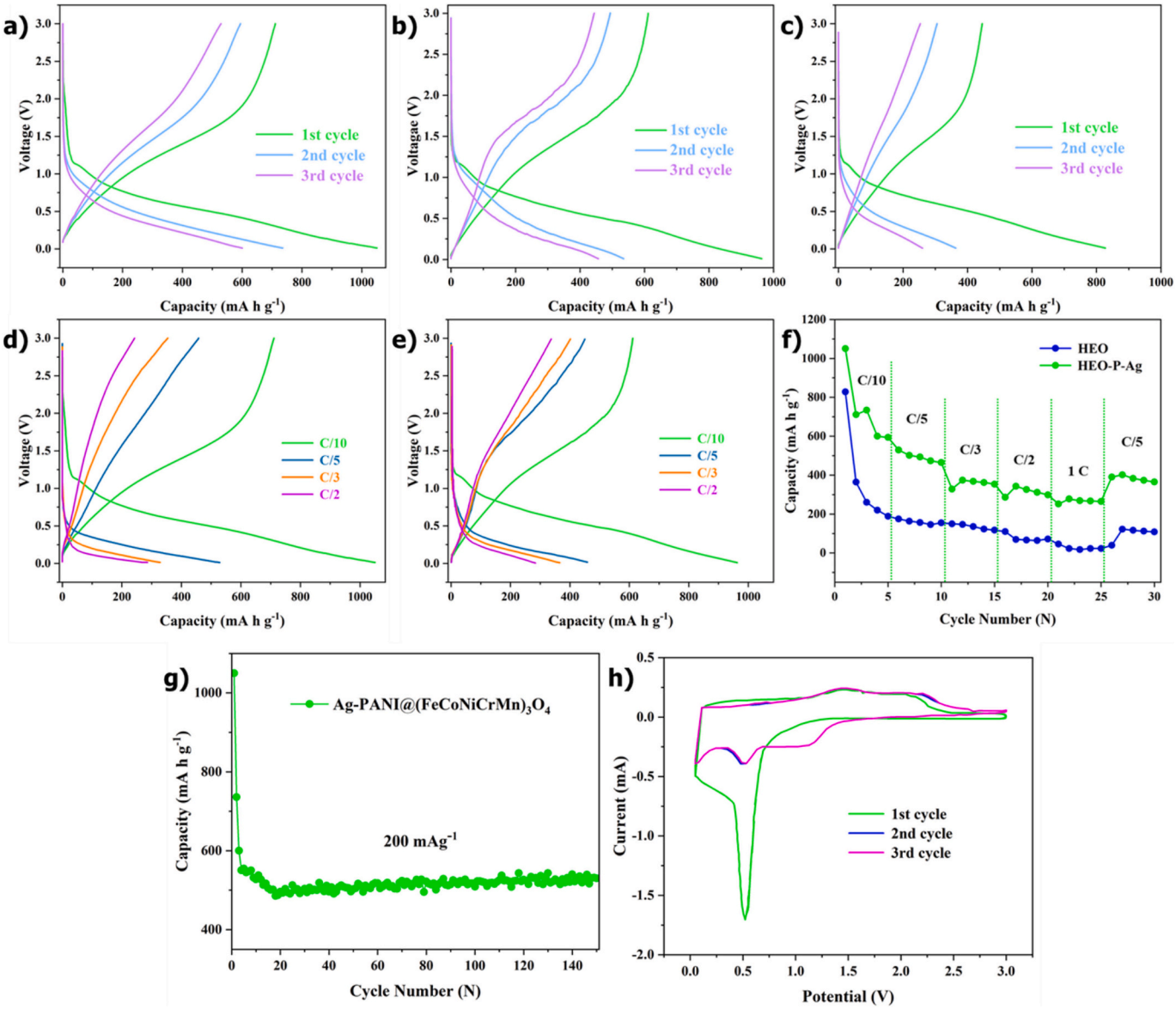

Fig. 6. Electrochemical Li^+ storage performance of spinel-based electrodes: (a)–(c) Initial charge–discharge curves at C/10 for HEO-P-Ag, HEO—P, and HEO, respectively; (d), (e) galvanostatic charge/discharge curves of HEO-P-Ag and HEO-P at various current densities; (f) rate capabilities of HEO and HEO-P-Ag electrodes at different specific currents; (g) long-term cycling performance of HEO-P-Ag at 200 mA g^{-1}; (h) cyclic voltammetry curves of HEO-P-Ag for the first three cycles at 0.1 m*V* s^{-1}.

practical values of charge transfer resistance are 74.34, 227.60, and 362.70 Ω for HEO-P-Ag, HEO—P, and HEO, respectively. Notably, the HEO-P-Ag electrode exhibits the lowest charge transfer impedance among the three samples, indicating that the introduction of Ag into the HEO structure effectively reduced Li^+ transport barrier. Fig. 7(b) illustrates the relationship between the real resistance ($Z^{'}$) and the inverse square root of frequency ($\omega^{-1/2}$) for HEO-P-Ag and HEO electrodes prior to cycling. Previous reports [45] have shown that a low slope in the fitted curve is indicative of rapid Li-ion diffusion within electrode materials, which can enhance the lithium storage performance of HEO-P-Ag.

The diffusion coefficient (D_{Li^+}) of Li^+ into the electrodes can be estimated using Eqs. (2) and (3) [46–50]:

$$D_{Li^+} = \frac{R^2T^2}{2A^2n^4F^4C^2\sigma_w^2} \quad (2)$$

$$Z_{real} = R_s + R_{ct} + \sigma_w\omega^{-1/2} \quad (3)$$

where *R* is the gas constant, *T* is the test temperature, *A* represents the electrode area, *n* is the number of electrons transferred per molecule, *F* represents the Faraday constant, *C* is the concentration of lithium ion in the electrolyte, R_S is the ohmic resistance of the battery system, R_{ct} is the charge-transfer resistance, ω represent the angular frequency, and σ_w is Warburg coefficient, determined by the slope of the fitting linear of $Z^{'}$-$\omega^{-1/2}$.

The lithium-ion diffusion coefficients and impedances are summarized in Table 2. HEO-P-Ag exhibits a lithium-ion diffusion coefficient approximately 2.73 times higher than that of HEO, representing a significant achievement. With an impedance of 74.34 Ω and a lithium-ion diffusion coefficient of 22.63 × 10^{-16} cm^2 s^{-1}, HEO-P-Ag outperforms both HEO-P (227.60 Ω, 14.33 × 10^{-16} cm^2 s^{-1}) and HEO (362.70 Ω, 8.28 × 10^{-16} cm^2 s^{-1}).

These results suggest that the Ag-modified PANI coating not only improves the conductivity of the HEO-P-Ag electrode materials but also accelerates charge transfer. The synergistic interaction between the

Table 1
Comparison of electrochemical performance of HEO-based anode materials for LIBs.

Material	Method	Specific capacity (mA h g^{-1})	Rate capability (mA h g^{-1})	Ref.
$(FeNiCrMnMgAl)_3O_4$	Solid-state reaction	555.79 @ 200 mA g^{-1}	436.11 @ 1 A g^{-1}	[37]
$(NiMnCrCoFe)_3O_4$	Hydrothermal	527.9 @ 5 A g^{-1}	568 @ 5 A g^{-1}	[38]
$(FeCoNiCrMn)_3O_4$	Solid-state reaction	612.3 @ 500 mA g^{-1}	600 @ 2 A g^{-1}	[39]
$(FeCoNiCuZnMgO_{1-x})$	Solution precursor plasma spraying	820.1 @ 100 mA g^{-1}	247.3 @ 2 A g^{-1}	[40]
(MgFeCoNiZn)O	Solid-state reaction	820 @ 50 mA g^{-1}	304 @ 0.5 A g^{-1}	[41]
$(TiFeCoNiZn)_3O_4$	Solid-state reaction	805 @ 50 mA g^{-1}	246 @ 0.5 A g^{-1}	[41]
$(CrMnCoNiZn)_3O_4$	Sol–gel	1388 @ 100 mA g^{-1}	96 @ 2 A g^{-1}	[42]
$(MgTiZnNiFe)_3O_4$	Solid-state reaction	424.7 @ 100 mA g^{-1}	93.6 @ 1 A g^{-1}	[43]
$(CrNiMnFeCu)_3O_4$	Hydrothermal	800 @ 50 mA g^{-1}	480 @ 2 A g^{-1}	[44]
Ag-PANI@ $(FeCoNiCrMn)_3O_4$	Solid-state reaction	1050.8 @ 200 mA g^{-1}	252 @ 2 A g^{-1}	This study

high-entropy oxide material and the Ag-modified PANI surface significantly enhances the electrochemical properties of HEO-P-Ag. It is always of crucial importance to take syntergitic reaction when it comes to charge transfer [51–53]. Additionally, the exceptional electrical conductivity of HEO-P-Ag is instrumental in achieving its high capacity and superior rate performance. Future studies will incorporate X-ray photoelectron spectroscopy (XPS) to probe the detailed chemical bonding states and oxidation changes of Ag and PANI on the HEO surface. This advanced surface characterization will allow for a more comprehensive understanding of the synergistic interactions, particularly in terms of the anchoring effect and conductive network formation.

To further examine the changes in surface morphology, coin-type half cells were disassembled after 30 cycles, and the HEO and HEO-P-Ag electrodes were extracted, cleaned with acetone, and dried for FESEM analysis. Fig. 8 clearly displays the evolution of the surface morphology for both the HEO and HEO-P-Ag anodes. Initially, as shown in Fig. 8(a) and (d), the pristine HEO and HEO-P-Ag anodes present relatively smooth surface structures. However, a closer examination reveals that the recycled HEO electrode, shown in Fig. 8(b) exhibits significant cracking and fragmentation from a continuous film to island-like structures. This indicates that long-term cycling-induced stresses significantly affect the surface morphology of the HEO anode. The increased spacing between cracks may lead to a loss of contact between the electrode and the current collector, which could contribute to a reduction in capacity. However, as illustrated in Fig. 8(e) and (f), the morphology of HEO-P-Ag remains largely stable, with no evidence of catastrophic pulverization. This stability can be attributed to the anchoring effect of the Ag-modified PANI layer. This suggests that the HEO-P-Ag structures are effectively preserved during charge/discharge processes, owing to the addition of the external PANI-Ag layer. Moreover, the primary role of the thin PANI-Ag layer is to isolate the electrolyte from the HEO particles, which reduces side reactions between these components, promotes the formation of a stable SEI layer, and thus increasing Li utilization. Given that HEOs function as conversion-type anodes, their conversion mechanism involves a reaction with Li that produces the corresponding reduced metals and Li_2O. Subsequently, lithium oxide can decompose into metal and oxygen, facilitating Li cycling and providing significant reversible capacity at suitable potentials.

The reaction mechanism of the discharge-charge process can be summarized as Reactions (4) and (5) [13]:

$$M_2O_3 + MO_2 + 4Li^+ \rightarrow 3MO + 2Li_2O, \quad (4)$$

$$MO + Li^+ \rightarrow M + Li_2O \quad (5)$$

$(M = Fe, Co, Ni, Cr \text{ and } Mn).$

Additionally, as depicted in Reaction (6), electrolyte ($LiPF_6$) interacts with trace amounts of water during charge and discharge cycles, resulting in the formation of non-conductive LiF impurities. The excessive accumulation of LiF within the SEI impedes Li^+ transport and increases resistance. Furthermore, HF dissolves transition metals present in HEO and reacts with Li_2O, as shown in Reactions (6) and (7):

$$LiPF_6 + H_2O \rightleftharpoons LiF + POF_3 + 2HF \quad (6)$$

Table 2
The list of R_S, R_{ct}, slope values, and D_{Li^+} of HEO, HEO—P, and HEO-P-Ag.

Sample	HEO	HEO-P	HEO-P-Ag
R_S	1.81	2.16	2.37
R_{ct}	362.70	227.60	74.34
Slope value (σ_w)	255.25	194.07	154.45
D_{Li^+} ($cm^2\ s^{-1}$, $\times 10^{-16}$)	8.28	14.33	22.63

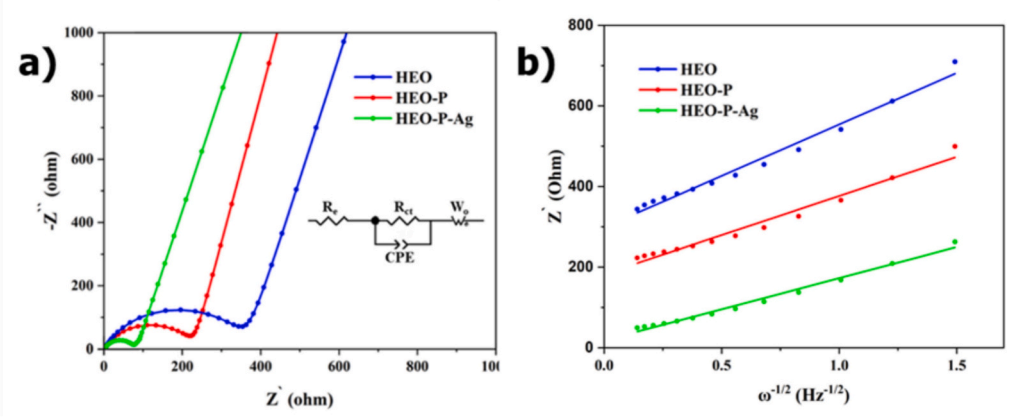

Fig. 7. (a) Nyquist plots of HEO electrodes and (b) plots of Z' versus $\omega^{-1/2}$.

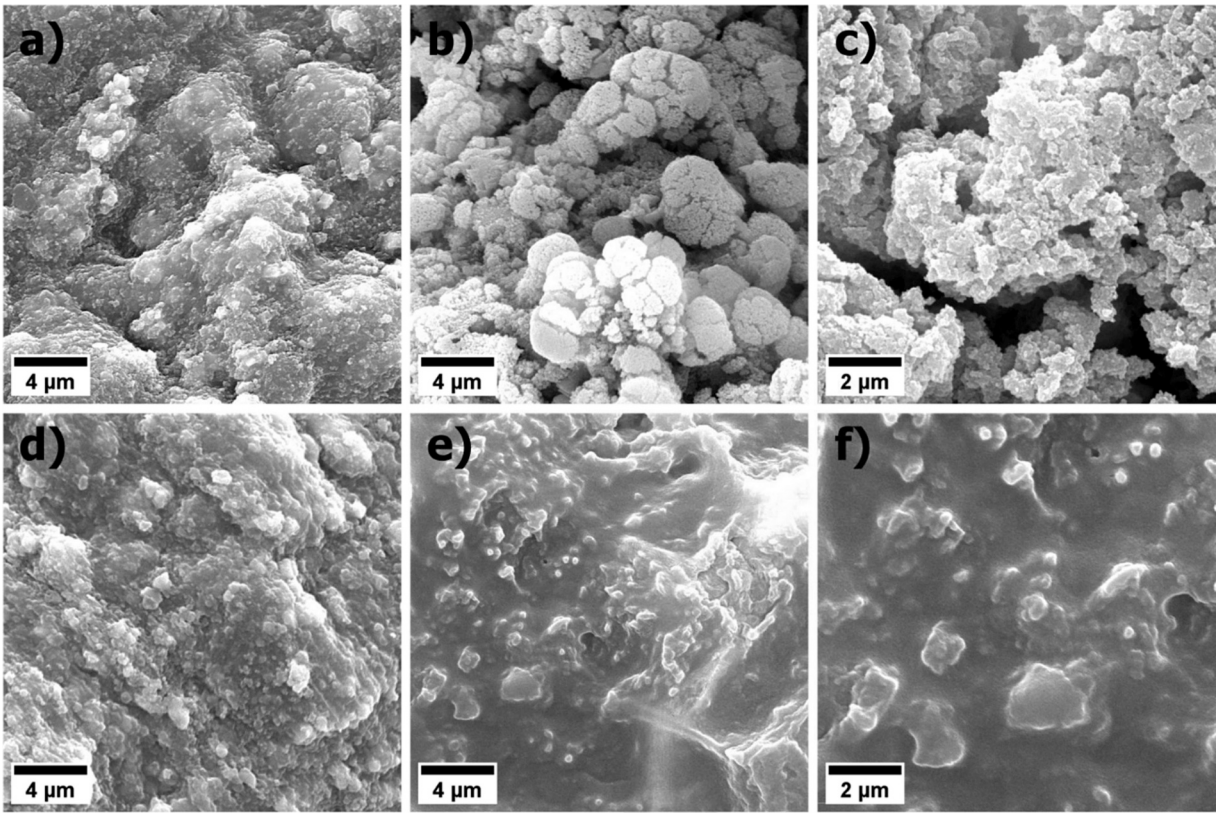

Fig. 8. FESEM images of (a) the HEO anode before lithiation, (b, c) the HEO anode after lithiation, and (d) the HEO-P-Ag anode before lithiation, (e, f) after lithiation.

$$Li_2O + 2HF \rightarrow 2LiF + 2H_2O \quad (7)$$

The formation of cracks and eventual rupture of the SEI leads to an increased contact area between the electrolyte and material, causing unstable SEI and the byproduct HF. The PANI-Ag layer offers several key advantages that enhance performance. Firstly, this thin layer serves to minimize direct contact between the electrolyte and material, thereby preventing the continuous accumulation of poorly conductive impurities. Furthermore, the reduced resistance of HEO-P-Ag in EIS (Fig. 7 (a)) indicates that there are fewer non-conductive components in the SEI. Secondly, the PANI-Ag layer plays a crucial role in facilitating electron transport between materials and effectively encapsulates refined HEO, thereby enhancing its overall stability and performance.

The observed morphological stability of the HEO-P-Ag electrode can be attributed to the mechanical buffering capability of the PANI layer, which accommodates the strain associated with volume fluctuations during charge/discharge cycles. Additionally, the presence of Ag nanoparticles reinforces the coating and improves its adhesion to the HEO surface, thereby further suppressing structural degradation. This synergistic effect helps maintain particle integrity, limits crack formation, and sustains electrode–electrolyte contact over prolonged cycling.

4. Conclusions

In this study, high-entropy oxide (HEO) anodes were synthesized using a conventional solid-state method, resulting in a single-phase spinel crystal structure with potential applications in lithium-ion batteries (LIBs). X-ray diffraction (XRD) analysis confirmed the successful formation of single-phase $(FeCoNiCrMn)_3O_4$ at 900 °C. Additionally, HEO-P-Ag was fabricated by modifying the surface of HEO with polyaniline (PANI) and silver (Ag). The combined effects of the spinel structure and the PANI-Ag layer facilitated ion/electron transfer while reducing damage to the electrode material caused by volume expansion during cycling. Consequently, HEO-P-Ag demonstrated exceptional lithium storage properties, outperforming HEO in both cycling stability and rate capability. Specifically, HEO-P-Ag displayed a high reversible capacity of 1050.8 mA h g^{-1} at a C-rate of C/10. Furthermore, it achieved a reversible capacity of 265 mA h g^{-1} at a high C-rate of 1C. The EIS results, including R_{ct}, and D_{Li^+}, revealed that the presence of the protective PANI-Ag layer significantly enhanced electron/ion transport kinetics in HEO-P-Ag.

Overall, this study offers valuable insights into the development of a promising anode material characterized by high reversible capacity, long-term cycling stability, and excellent rate performance for LIB applications.

CRediT authorship contribution statement

Arezoo Jari: Writing – original draft, Visualization, Validation, Methodology, Formal analysis, Conceptualization. **Abbas Bahrami:** Writing – review & editing, Visualization, Validation, Supervision, Project administration, Investigation, Funding acquisition, Formal analysis. **Masoud Panjepour:** Writing – original draft, Supervision, Project administration, Methodology, Investigation, Funding acquisition. **Maryam Yazdan Mehr:** Writing – original draft, Resources, Methodology, Investigation.

Declaration of competing interest

The authors declare that they have no known competing financial interests or personal relationships that could have appeared to influence the work reported in this paper.

References

[1] L. Zhou, L. Xie, J. Dai, A. Jain, G. Chen, Y. Zhao, Orthogonal test–based design and optimization of a Li-Ion battery thermal management system with a liquid-cooled reverse parallel structure and Inlaid Fins, Asia Pac. J. Chem. Eng. (2025) e70056.

[2] C. Liu, L. Sheng, L. Jiang, Research on performance constraints and electrolyte optimization strategies for lithium-ion batteries at low temperatures, RSC Adv. 15 (10) (2025) 7995–8018.

[3] L. Tong, Y. Li, Y. Xu, J. Fang, C. Wen, Y. Zheng, H. Zhang, B. Peng, F. Yang, J. Zhang, M. Gong, A combined method for state-of-charge estimation for lithium-ion batteries based on IGWO-ASRCKF and ELM under various aging levels, J Energy Storage 124 (2025) 116843.

[4] Y.-K. Sun, Z. Chen, H.-J. Noh, D.-J. Lee, H.-G. Jung, Y. Ren, S. Wang, C.S. Yoon, S.-T. Myung, K. Amine, Nanostructured high-energy cathode materials for advanced lithium batteries, Nat. Mater. 11 (2012) 942–947.

[5] M.M. Bidwe, S.G. Kulkarni, Lithium-ion battery: a review, Int. J. Veh. Inf. Commun. Syst. 9 (2) (2024) 135–163.

[6] J. Liu, Y. Xu, F. Xu, J. Li, Y. Chen, J. Qiao, Y. Han, Y. Ren, B. Lin, Zwitterionic poly (ionic liquids)-based polymer electrolytes for Lithium-ion batteries applications, Ionics 29 (6) (2023) 2249–2259.

[7] R. Van Noorden, A better battery, Nature 507 (2014) 26.

[8] V. Etacheri, R. Marom, R. Elazari, G. Salitra, D. Aurbach, Challenges in the development of advanced Li-ion batteries: a review, Energy Environ. Sci. 4 (2011) 3243–3262.

[9] M.T. McDowell, S.W. Lee, W.D. Nix, Y. Cui, 25th anniversary article: understanding the lithiation of silicon and other alloying anodes for lithium-ion batteries, Adv. Mater. 25 (2013) 4966–4985.

[10] J. Asenbauer, T. Eisenmann, M. Kuenzel, A. Kazzazi, Z. Chen, D. Bresser, The success story of graphite as a lithium-ion anode material–fundamentals, remaining challenges, and recent developments including silicon (oxide) composites, Sustain. Energy & Fuels 4 (2020) 5387–5416.

[11] C.M. Rost, E. Sachet, T. Borman, A. Moballegh, E.C. Dickey, D. Hou, J.L. Jones, S. Curtarolo, J.-P. Maria, Entropy-stabilized oxides, Nat. Commun. 6 (2015) 1–8.

[12] A. Sarkar, L. Velasco, D. Wang, Q. Wang, G. Talasila, L.D. Biasi, T. Brezesinski, S. S. Bhattacharya, H. Hahn, B. Breitung, High entropy oxides for reversible energy storage, Nat 9 (2018) 3400.

[13] B. Xiao, G. Wu, T. Wang, Z. Wei, Y. Sui, B. Shen, J. Qi, F. Wei, J. Zheng, High-entropy oxides as advanced anode materials for long-life lithium-ion batteries, Nano Energy 95 (2022) 106962.

[14] L. Dong, Y. Tian, C. Luo, W. Zhao, C. Qin, Z. Wang, Porous high-entropy oxide anode materials for Li-ion batteries: preparation, characterization, and applications, Materials 17 (2024) 1542.

[15] Y. Zheng, X. Wu, X. Lan, R. Hu, A spinel (FeNiCrMnMgAl) 3O4 high entropy oxide as a cycling stable anode material for Li-ion batteries, Processes 10 (2021) 49.

[16] K. Wang, W. Hua, X. Huang, D. Stenzel, J. Wang, Z. Ding, Y. Cui, Q. Wang, H. Ehrenberg, B. Breitung, C. Kübel, X. Mu, Synergy of Cations in High Entropy Oxide Lithium Ion Battery Anode, 2023, pp. 1–9, https://doi.org/10.1038/s41467-023-37034-6.

[17] J. Yeh, S. Chen, S. Lin, J. Gan, T. Chin, T. Shun, C. Tsau, S. Chang, Nanostructured high-entropy alloys with multiple principal elements: novel alloy design concepts and outcomes, Adv. Eng. Mater. 6 (2004) 299–303.

[18] Y. Zhang, T.T. Zuo, Z. Tang, M.C. Gao, K.A. Dahmen, P.K. Liaw, Z.P. Lu, Microstructures and properties of high-entropy alloys, Prog. Mater. Sci. 61 (2014) 1–93.

[19] M.-H. Tsai, J.-W. Yeh, High-entropy alloys: a critical review, Mater. Res. Lett. 2 (2014) 107–123.

[20] D.B. Miracle, O.N. Senkov, A critical review of high entropy alloys and related concepts, Acta Mater. 122 (2017) 448–511.

[21] H. Wu, G. Yu, L. Pan, N. Liu, M.T. McDowell, Z. Bao, Y. Cui, Stable Li-ion battery anodes by in-situ polymerization of conducting hydrogel to conformally coat silicon nanoparticles, Nat. Commun. 4 (2013) 1943.

[22] X. Yang, X. Liu, T. Qin, X. Zhang, W. Zhang, W. Zheng, Polypyrrole coated hollow S/Co-doped carbon nanocages excels for packaging high-performance lithium sulfur batteries, Nanotechnology 31 (2020) 275404.

[23] Y. Luo, R. Guo, T. Li, F. Li, Z. Liu, M. Zheng, B. Wang, Z. Yang, H. Luo, Y. Wan, Application of polyaniline for Li-ion batteries, lithium–sulfur batteries, and supercapacitors, ChemSusChem 12 (2019) 1591–1611.

[24] L. Yang, H. Liao, Y. Tian, W. Hong, P. Cai, C. Liu, Y. Yang, G. Zou, H. Hou, X. Ji, Rod-like Sb2MoO6: structure evolution and sodium storage for sodium-ion batteries, Small Methods 3 (2019) 1800533.

[25] K.-J. Jeong, T.J. Wang, H.H. Nersisyan, J.H. Han, J.H. Lee, Tailored silver nanowires for amplified Lithium-ion battery performance and inhibition of Lithium dendrites in silicon–graphite–silver nanowire composite electrodes, ACS Appl Energy Mater 6 (2023) 11626–11641.

[26] Y. Gao, B.-F. Cui, J.-J. Wang, Z.-Y. Sun, Q. Chen, Y.-D. Deng, X.-P. Han, W.-B. Hu, Improving Li reversibility in Li metal batteries through uniform dispersion of ag nanoparticles on graphene, Rare Metals 41 (2022) 3391–3400.

[27] R.-Z. Zhang, M.J. Reece, Review of high entropy ceramics: design, synthesis, structure and properties, J Mater Chem A 7 (2019) 22148–22162.

[28] H. Minouei, N. Tsvetkov, M. Kheradmandfard, J. Han, D.-E. Kim, S.I. Hong, Tuning the electrochemical performance of high-entropy oxide nanopowder for anode Li-ion storage via structural tailoring, J. Power Sources 549 (2022) 232041.

[29] Y. Li, Z. Chen, J. Liu, R. Liu, C. Zhang, H. Li, Novel high entropy oxide as anode for high performance lithium-ion capacitors, Ceram. Int. 49 (2023) 38439–38447.

[30] X. Liu, Y. Yu, K. Li, Y. Li, X. Li, Z. Yuan, H. Li, H. Zhang, M. Gong, W. Xia, Intergrating hollow multishelled structure and high entropy engineering toward enhanced mechano-electrochemical properties in lithium battery, Adv. Mater. 36 (2024) 2312583.

[31] G. Liang, Z. Wu, C. Didier, W. Zhang, J. Cuan, B. Li, K. Ko, P. Hung, C. Lu, Y. Chen, A long cycle-life high-voltage spinel lithium-ion battery electrode achieved by site-selective doping, Angew. Chem. 132 (2020) 10681–10689.

[32] Y. Yeh, C. Huang, A. Hou, C. Huang, Y. Lin, W. Wu, In Situ TEM observation of (Cr, Mn, Fe, Co, and Ni) 3O4 high-entropy spinel oxide formation during calcination at atomic scale, Small 20 (2024) 2307284.

[33] Y. Wang, W. Wu, L. Cheng, P. He, C. Wang, Y. Xia, A polyaniline-intercalated layered manganese oxide nanocomposite prepared by an inorganic/organic Interface reaction and its high electrochemical performance for Li storage, Adv. Mater. 20 (2008) 2166–2170.

[34] C. Murugan, E. Subramanian, D.P. Padiyan, P–n heterojunction formation in polyaniline–SnO2 organic–inorganic hybrid composite materials leading to enhancement in sensor functionality toward benzene and toluene vapors at room temperature, Synth. Met. 192 (2014) 106–112.

[35] R. Mohammadzadeh Kakhki, S. Hedayat, K. Mohammadzadeh, Novel, green and low cost synthesis of ag nanoparticles with superior adsorption and solar based photocatalytic activity, J. Mater. Sci. Mater. Electron. 30 (2019) 8788–8795.

[36] L. Yin, M. Park, I. Jeon, J.H. Hwang, J.P. Kim, H.W. Lee, M. Park, S.Y. Jeong, C.-R. Cho, Silicon nanoparticle self-incorporated in hollow nitrogen-doped carbon microspheres for lithium-ion battery anodes, Electrochim. Acta 368 (2021) 137630.

[37] X. Guo, P. Gu, J. Wu, K. Li, Y. Liang, G. Wang, Z. Zhang, C. Guo, A novel co-free high-entropy oxide (FeNiCrMnMgAl) 3O4 as advanced anode material for lithium-ion batteries, J. Electroanal. Chem. 978 (2025) 118910.

[38] X.L. Wang, E.M. Jin, G. Sahoo, S.M. Jeong, High-entropy metal oxide (NiMnCrCoFe) 3O4 anode materials with controlled morphology for high-performance lithium-ion batteries, Batteries 9 (2023) 147.

[39] F. Zhai, X. Zhu, W. Zhang, G. Cao, H. Zhang, Y. Xing, Y. Xiang, S. Zhang, Insight of the evolution of structure and energy storage mechanism of (FeCoNiCrMn) 3O4 spinel high entropy oxide in life-cycle span as lithium-ion battery anode, J. Power Sources 603 (2024) 234418.

[40] Y. Lin, S. Chen, Y. Ma, S. Wang, Z. Ma, L. Sun, R. Cao, G. Song, Z. Yu, J. Yao, One-step, binder-free and rapid synthesis of high-entropy oxide anode materials for the lithium-ion batteries, Next Mater. 8 (2025) 100855.

[41] O.J.B.J. Marques, M.D. Walter, E.V. Timofeeva, C.U. Segre, Effect of initial structure on performance of high-entropy oxide anodes for li-ion batteries, Batteries 9 (2023) 115.

[42] C. Jin, Y. Wang, H. Dong, Y. Wei, R. Nan, Z. Jian, Z. Yang, Q. Ding, A novel spinel high-entropy oxide (Cr0. 2Mn0. 2Co0. 2Ni0. 2Zn0. 2) 3O4 as anode material for lithium-ion batteries, Inorganics 12 (2024) 198.

[43] C. Liu, J. Bi, L. Xie, X. Gao, L. Meng, Preparation and electrochemical properties of two novel high entropy spinel oxides (MgTiZnNiFe) 3O4 and (CoTiZnNiFe) 3O4 by solid state reaction, Mater Today Commun 35 (2023) 106315.

[44] J. Patra, T.X. Nguyen, C. Tsai, O. Clemens, J. Li, P. Pal, W.K. Chan, C. Lee, H. T. Chen, J. Ting, Effects of elemental modulation on phase purity and electrochemical properties of co-free high-entropy spinel oxide anodes for Lithium-ion batteries, Adv. Funct. Mater. 32 (2022) 2110992.

[45] L. Fu, K. Tang, K. Song, P.A. van Aken, Y. Yu, J. Maier, Nitrogen doped porous carbon fibres as anode materials for sodium ion batteries with excellent rate performance, Nanoscale 6 (2014) 1384–1389.

[46] Y. Zhang, X. Qin, Y. Liu, Y. Chen, C. Lei, T. Wei, Novel Si@ C/P anode materials with improved cyclability and rate capacity for lithium-ion batteries, J. Alloys Compd. 899 (2022) 163237.

[47] H. Guo, J. Shen, T. Wang, C. Cheng, H. Yao, X. Han, Q. Zheng, Design and fabrication of high-entropy oxide anchored on graphene for boosting kinetic performance and energy storage, Ceram. Int. 48 (2022) 3344–3350.

[48] H. Chen, N. Qiu, B. Wu, Z. Yang, S. Sun, Y. Wang, A new spinel high-entropy oxide (Mg0.2Ti0.2Zn0.2Cu0.2Fe0.2)3O4 with fast reaction kinetics and excellent stability as an anode material for lithium ion batteries, RSC Adv. 10 (2020) 9736–9744.

[49] K.F. Zare, A. Eslami, A. Bahrami, Characterization and performance of graphite–lithium titanium oxide composites used as anodes in lithium-ion batteries, Arab. J. Sci. Eng. (2025) 1–21.

[50] A. Jari, M. Panjepour, A. Bahrami, M. Yazdan Mehr, Synthesis, characterization, and evaluation of polyaniline-modified (FeCoNiCrMn)3O4 high-entropy oxide as an anode material for lithium-ion batteries, Mater. Chem. Phys. 333 (2025) 130322.

[51] S. Yu, K. Cai, H. Zhao, T. Wang, T. Qu, L. Li, J. Li, C. Yao, X. Lang, Adjusting the electron configuration of MOFs-derived Ag/MnO1.1@C via electron transfer strategy to achieve a high-performance catalyst for potassium-oxygen batteries, Appl. Surf. Sci. 709 (2025) 163863.

[52] Z. Li, L. Gao, C. Zhang, F. Li, Copper incorporation induced oxygen vacancy MoO3 anode and Zn dendrite inhibitor for high performance aqueous zinc ion batteries, J Energy Storage 119 (2025) 116336.

[53] C. Wang, Y. Zhu, T. Zhang, J. Tian, F. Gao, Y. Zhao, X. Bu, T. Quan, Competition between discharge reaction and side reaction for anode's lithium during internal short circuit in lithium-ion batteries, J. Clean. Prod. 470 (2024) 143280.